

## Seismic evidence for variations in axial magma chamber properties along the southern Juan de Fuca Ridge

J. Pablo Canales <sup>a,\*</sup>, Satish C. Singh <sup>b</sup>, Robert S. Detrick <sup>a</sup>, Suzanne M. Carbotte <sup>c</sup>,  
Alistair Harding <sup>d</sup>, Graham M. Kent <sup>d</sup>, John B. Diebold <sup>c</sup>,  
Jeffrey Babcock <sup>d</sup>, Mladen R. Nedimović <sup>c</sup>

<sup>a</sup> Department of Geology and Geophysics, MS#24, Woods Hole Oceanographic Institution, 360 Woods Hole Rd., Woods Hole, MA 02543, USA

<sup>b</sup> Laboratoire de Géosciences Marines, Institut de Physique du Globe de Paris, France

<sup>c</sup> Lamont-Doherty Earth Observatory, Palisades, NY, USA

<sup>d</sup> Scripps Institution of Oceanography, La Jolla, CA, USA

Received 10 October 2005; received in revised form 3 April 2006; accepted 23 April 2006

Editor: R.D. van der Hilst

### Abstract

Multichannel seismic data collected along the Cleft segment on the southern Juan de Fuca Ridge show that this intermediate-spreading center is underlain by a mid-crustal reflector interpreted as the top of an axial magma chamber (AMC). The AMC reflection is present along most of the segment, and deepens gently from 2.0 km near the southern end of the segment beneath the RIDGE Cleft Observatory Site, to 2.3 km at the northern end beneath the site of the mid-1980s submarine eruption. We analyzed the one-dimensional seismic structure of the AMC at two locations with contrasting lava chemistry beneath two different hydrothermal vent fields. At the northern site, waveform modeling in the time intercept–slowness ( $\tau$ - $p$ ) domain indicates that the AMC is ~100 m thick and it is characterized by a decrease in  $P$ -wave velocity from 6 km/s to 3.7 km/s. In contrast, the  $P$ -wave velocity within the shallower, ~100-m-thick AMC at the southern site is higher (5.0 km/s). The decrease in seismic velocity within the AMC indicates that it is partially molten and that it is not a cracking front as previously suggested for other intermediate-spreading segments. The data show a coherent seismic phase interpreted as the  $P$ - to  $S$ -wave conversion at the AMC ( $P_{AMC}S$ ). Stacking of this event shows that the  $P_{AMC}S$  is only present along the northern part of the segment. Our results thus suggest along-axis variations in the crystallinity of the AMC. The AMC along Cleft varies from a high crystal content (<30% melt) sill at the southern end of Cleft, to a largely melt (60–75%) sill at the source of the 1980s eruption at the northern end. The variations in magma chamber properties inferred from our seismic data correlate with changes in lava chemistry and with the location of hydrothermal plumes, and they all suggest that focused, high-temperature hydrothermal venting along intermediate-spreading ridges is closely linked to the physical state of the underlying magma chamber.

© 2006 Elsevier B.V. All rights reserved.

**Keywords:** Juan de Fuca Ridge; Cleft segment; magma chamber; seismic structure; hydrothermal activity

\* Corresponding author. Tel.: +1 508 289 2893; fax: +1 508 457 2150.

E-mail address: [jpcanales@whoi.edu](mailto:jpcanales@whoi.edu) (J.P. Canales).

## 1. Introduction

Seismic studies along intermediate-spreading centers (e.g., [1–7]) have shown that a significant portion of these ridges is characterized by a mid-crustal reflector with some of its characteristics (e.g., along-axis continuity, width) similar to those of the axial magma chamber (AMC) reflector observed along the fast-spreading East Pacific Rise (EPR) (e.g., [8]). In back-arc ridges spreading at intermediate rates, this reflector represents the top of a partially molten AMC of andesitic melts with high volatile content (e.g., [7,9]). However, the nature of this reflector at intermediate-spreading ridges away from hot spots and arc influences has not been firmly established yet, and some authors have argued that at least at some intermediate-spreading segments, the mid-crustal axial reflector could be associated with a downward-propagating cracking front rather than with the top of an AMC [10]. Crustal accretion processes along intermediate-spreading ridges are highly sensitive to changes in the thermal balance between heat input from magma chambers and heat extraction by hydrothermal circulation (e.g., [11]). Therefore, understanding the nature and physical state of the axial mid-crustal reflector observed at intermediate-spreading ridges has important implications for seafloor eruption processes and the chemistry of the lavas originated at these mid-ocean ridges (e.g., [12]), as well as for discriminating between alternative models for the driving force of mid-ocean ridge high-temperature hydrothermal circulation (i.e., latent heat from crystallization of magma chambers versus specific heat extracted from hot but un-molten rocks) (e.g., [13]).

At the well-studied EPR, the AMC is characterized by a decrease in seismic velocity resulting from the impedance contrast between a ~50-m-thick solid roof (that separates the magma chamber from the upper crustal hydrothermal fluids) and a thin (~30–100 m) sill of melt and crystals (e.g., [14–17]). The properties (i.e., crystallinity) of the AMC at the EPR vary along axis; with 2- to 4-km-long sills of pure melt ( $V_S=0$  km/s) embedded in a mush-rich ( $V_S>0$  km/s) matrix [16]. At the intermediate-spreading, back-arc Valu Fa Ridge the AMC represents a decrease in seismic velocity at 3.2 km below the seafloor (bsf), and the along-axis variations in reflection strength have been interpreted to result from changes in melt body thickness rather than crystallinity [9]. Whether or not the mid-crustal axial reflector observed at intermediate-spreading ridges (hereinafter implicitly excluding hotspot and back-arc settings) is associated with a decrease in seismic velocity (as it would be the case for low velocity AMC), or a positive

impedance contrast (as predicted by the cracking front hypothesis) remains to be tested, as well as whether its properties are segmented and change at the same scale as at the EPR.

In this paper we address the above-mentioned questions by determining the seismic structure of the axial mid-crustal reflector observed along the intermediate spreading rate Cleft segment in the Southern Juan de Fuca Ridge (JdFR), as well as by imaging S-wave converted reflections from the axial reflector. Our results show striking correlations with existing petrological and hydrothermal data, and thus provide constraints on the linkages between magmatic and hydrothermal process at intermediate spreading ridges.

## 2. Geological and geophysical background

The JdFR is the boundary between the Pacific and Juan de Fuca plates (Fig. 1). Its southernmost segment (Cleft) has a full spreading rate of 56 mm/yr [18]. The ~60-km-long Cleft segment is bounded on the south by the Blanco fracture zone, and to the north by the Vance segment, with which it overlaps for ~15 km near 45°05' N [19] (Fig. 1). The axis of the Cleft segment sits on an elevated, rifted axial high within a 2- to 4-km-wide, ~100-m-deep axial graben (e.g., [20]). Within the axial graben along the southern part of the Cleft segment, there is a 50- to 100-m-wide, 5- to 30-m-deep narrow depression or cleft that gives the segment its name [20–22]. The dimensions, shape, and volcanic and hydrothermal characteristics of this feature are identical to those of the axial summit collapse trough found along the EPR (e.g., [23,24]).

The southern part of the Cleft segment is characterized by a young, large sheet flow [19,22], and the presence of high-temperature hydrothermal vents [20,21]. It is also the site of the RIDGE Cleft Observatory [25,26] (Fig. 1). Towards the center of the segment, lavas are older and generally more tectonized (fractured sheet flows and constructional mounds). The northern part of the segment experienced an eruptive episode in the 1980s [27], and it is characterized by fresh, glassy sheet flows and pillow mounds, and both high- and low-temperature hydrothermal venting [28] (Fig. 1). Basalt samples along the axis of Cleft indicate that there are strong correlations between relative lava age, degrees of fractionation, and latitude [29], with younger looking and more primitive lavas found progressively towards the north [29,30]. Based on these observations, Smith et al. [29] suggest that lavas were derived from discrete magma lenses, each in different stage of evolution along the axis.

The presence of a crustal magma chamber along the axis of the Cleft segment was first suggested by Morton et al. [4], and it has been recently imaged and described in more detail by Canales et al. [3]. These authors attribute the axial crustal reflector to the top of the AMC; therefore hereinafter we will refer to it simply as the AMC. The AMC is present along ~60% of the Cleft axis, and is continuous along ~5- to 10-km-long sections of the segment. The AMC deepens from

south to north [3], from ~2.0 km below the seafloor at the southern end of the segment, to ~2.3 km at the northern end.

### 3. Waveform inversion

We have modeled the one-dimensional (1D) *P*-wave velocity structure of the AMC using recently collected multichannel seismic (MCS) reflection data gathered in

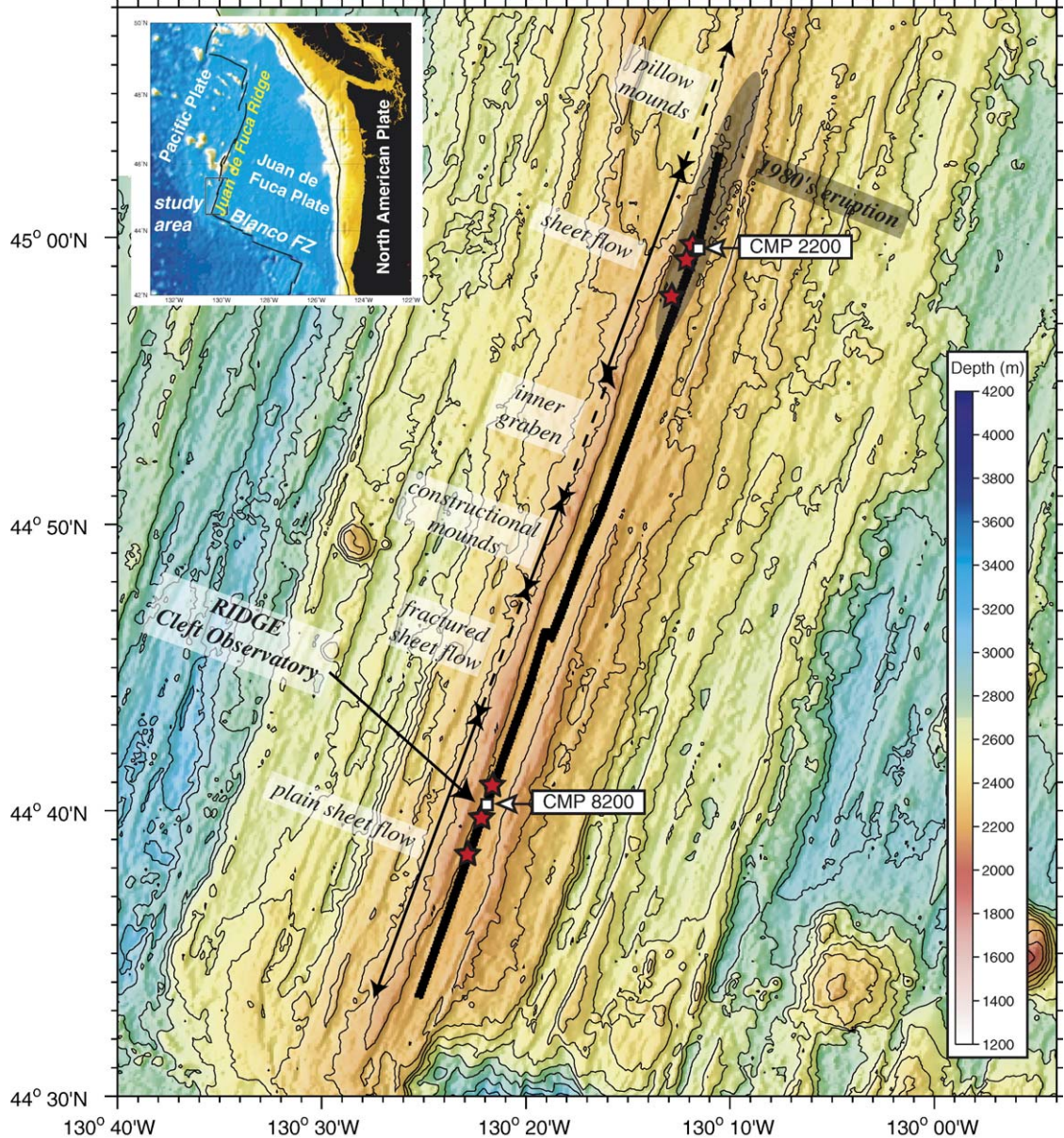


Fig. 1. Bathymetry map of the Cleft segment in the southern Juan de Fuca Ridge. Solid black line is the axial seismic reflection profile Line 80 [3]. Open squares indicate locations of CMP gathers 2200 and 8200 where the 1-D waveform modeling was performed (Figs. 2 and 3). Red stars show the location of known high-temperature hydrothermal vents, and gray zone near 45°00'N corresponds to the location of the 1980s eruption. Contours every 100 m, illumination from WNW. Lava morphologies are from Embley and Chadwick [19].

common mid points (CMP). Details on data acquisition parameters are given in Canales et al. [3]. To improve the signal-to-noise ratio, we constructed constant-offset stacks (super-CMP gathers) by combining 30 consecutive CMP gathers and stacking the 5-fold constant-offset traces. We have performed our analysis at two locations along the Cleft segment with contrasting lava chemistry [29] where the AMC is best imaged [3]: CMP 2200 near the site of the 1980s eruptive event, and CMP 8200 at the RIDGE Cleft Observatory Site (Fig. 1). At the northern site the AMC reflection is clearly observed as a nearly flat event at  $\sim 4$  s two-way travel time (twtt) (0.94 s below the zero-offset seafloor reflection) between 0 and 2.5 km offset (Fig. 2a). At the southern site that AMC is somewhat shallower (0.85 s bsf at zero offset) and is observed only up to  $\sim 1.5$  km offset (Fig. 2b).

We applied a waveform inversion scheme to find the 1D velocity structure that minimizes the misfit between the observed and predicted seismograms (e.g., [17]). The misfit is calculated in the frequency–slowness ( $\omega-p$ ) domain, hence the observed super-gathers have to be transformed, prior to the inversion, from the time–offset

( $t-x$ ) domain (Fig. 2a, b) to the delay time–slowness ( $\tau-p$ ) domain (Fig. 2c, d), and then Fourier-transformed to the  $\omega-p$  domain. We followed the  $\tau-p$  transformation method of Harding [31] (as implemented by Korenaga et al. [32]), a three-dimensional cylindrical-wave decomposition of the seismic data that accounts for phase shifts and geometrical spreading from a point source. The data were not corrected for source, receiver, and ghost directivity effects (e.g., [33]), which we calculated to be negligible. The data were band-pass filtered between 5, 10, 30, and 50 Hz. The transformed  $\tau-p$  gathers and the mapped AMC event are shown in Fig. 2c and d.

The waveform inversion is done in the  $\omega-p$  domain following the method of Kormendi and Dietrich [34], which solves the non-linear inverse problem using generalized least squares and minimizes the misfit function using the conjugate gradient algorithm. More details on the inversion procedure can be found in [17,32,34]. The inversion results are highly sensitive to the input source wavelet (e.g., [17]). Since we do not have information on the far-field response of the air-gun signal for our experiment, we need to obtain a realistic

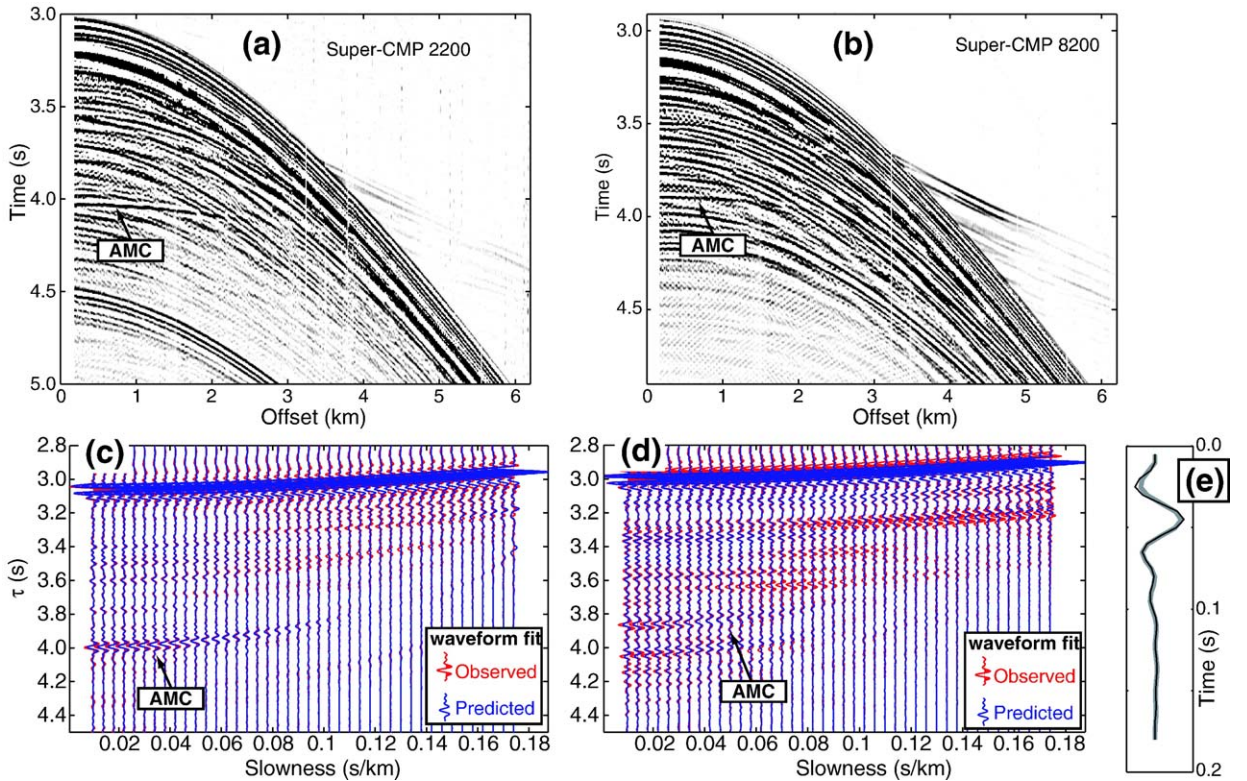


Fig. 2. Super-CMP gathers from the northern (a) and southern (b) ends of Cleft segment. (c), (d) Corresponding observed (red) and predicted (blue)  $\tau-p$  gathers. (e) Estimated source wavelets for CMP 2200 and 8200 (gray and solid black lines, respectively). These wavelets were derived from  $\tau-p$  data deconvolved with an initial estimate of the source wavelet (see text for details).

estimate of the source wavelet following indirect methods. We estimated an initial source wavelet by averaging 10  $\omega-p$  traces at the lowest slowness, and then transformed the resulting averaged spectrum back to the  $\tau-p$  domain (method 4 of Collier and Singh [17]). Because of the ringy character of the air-gun source, which is magnified by side-echoes from the rough seafloor, we deconvolved the  $\tau-p$  gathers with the estimated source wavelet to obtain sharper, cleaner  $\tau-p$  gathers (Fig. 2c, d). We then re-estimated the final source wavelet from the deconvolved  $\tau-p$  gathers (Fig. 2e).

As initial velocity model for the inversion, we used a model derived from forward modeling of crustal refraction and reflection travel times observed in shot gathers at the location of CMP 8200 [3]. For the inversion, the density and  $V_S$  structures were kept fixed during a few iterations (typically 5), and then updated

from the inverted  $V_P$  structure using a  $V_P$ -density relationship [35] (except at the seafloor and within the AMC where densities were fixed at  $2240 \text{ kg/m}^3$  [36] and  $2600 \text{ kg/m}^3$ , respectively) and assuming a Poisson's ratio of 0.48 for the upper 570 m and 0.25 everywhere else [37]. The  $P$ -wave attenuation quality factor was set to 16 in the upper 570 m, and 100 below this depth [38]. The  $S$ -wave attenuation quality factor was set to half of that of the  $P$ -wave.

Our preferred best-fitting models are shown in Fig. 3a, and the predicted seismograms in Fig. 2c, d. Our results show that at the southern end of Cleft segment, the AMC is characterized by a  $\sim 100\text{-m}$ -thick low velocity zone, with a decrease in  $V_P$  from  $\sim 6 \text{ km/s}$  to  $5.0 \text{ km/s}$  at  $1.9 \text{ km}$  depth. At the northern site, the AMC is also  $\sim 100 \text{ m}$  thick, but is located deeper ( $2.23 \text{ km}$ ) and shows a significantly larger decrease in  $V_P$  ( $3.7 \text{ km/s}$ ). The AMC depth is consistent with the estimates of

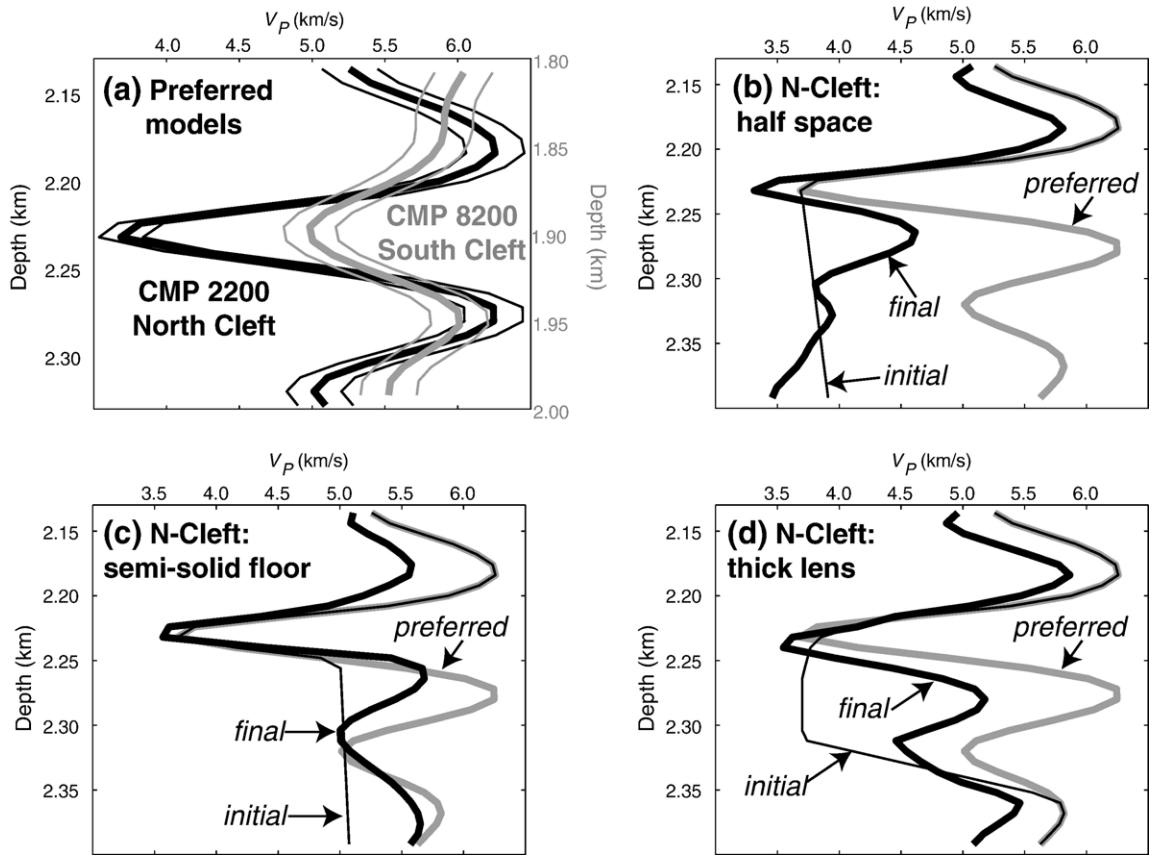


Fig. 3. (a) Preferred 1-D  $P$ -wave velocity models (thick lines) for the northern (black) and southern (gray) Cleft segment. Note the different vertical scales. The AMC in N-Cleft is deeper ( $2.23 \text{ km}$ ) and has lower  $V_P$  ( $3.7 \text{ km/s}$ ), while the AMC in S-Cleft is shallower ( $1.9 \text{ km}$ ) and has larger  $V_P$  ( $5.0 \text{ km/s}$ ). Thin lines show the preferred models  $\pm$  one standard deviation error estimated from the Hessian matrix. (b)–(d) Resolution tests of the structure of the melt lens floor at the northern Cleft site (CMP 2200); (b) a purely molten half space is used as initial model (thin line), thick black line shows the inversion result compared to our preferred model (gray line); (c) same as (b) with initial model assuming a partially molten floor; (d) same as (b) assuming a thick ( $\sim 200 \text{ m}$ ) melt lens as starting model.

Canales et al. [3] from seismic reflection images. The  $P$ -wave velocity of the AMC at both sites is within the range of velocities estimated along different areas of the EPR [14,16,17].

The preferred models have an uncertainty of  $\pm 0.15\text{--}0.20$  km/s (Fig. 3a), which is valid only if the starting model is close to the global minimum of the misfit function. Some of the features of the preferred models may be dependent on the initial assumptions and not fully required by the data. One important aspect is the thickness of the melt lens and the structure immediately beneath it. Previous studies at the southern EPR have shown that the melt lens is bounded by a solid roof and a solid floor [15]. We performed a series of resolution tests to investigate if our data require the presence of a solid floor (indicated by the relatively high  $V_p$  immediately beneath the low  $V_p$  melt lens, Fig. 3a). We inverted the data from CMP 2200 at the northern Cleft site using initial velocity models modified from the preferred solution: one where  $V_p$  is low everywhere beneath the top of the AMC (Fig. 3b), and a second one in which the velocity of the melt lens floor increases moderately, simulating a semi-solid floor (Fig. 3c). In both cases, the new inversions result in models that fit the data with the same degree of accuracy as the preferred solution. These tests show that our data cannot discriminate between a solid and a semi-solid floor, but that the data require an increase in  $V_p$  with respect to the initial velocity model immediately beneath the melt lens. We performed another test where we imposed a thicker ( $\sim 200$  m) AMC, and then inverted the data (Fig. 3d). The solution from this test shows that the data require a thin lens no more than 100 m thick. Thus, our tests indicate that the top of the AMC is a partially molten thin lens overlaying a more crystalline medium.

Our results clearly indicate that the physical properties of the AMC at both sites differ. However it is important to acknowledge and to keep in mind the assumptions we have made and the limitations of the method used. Mid-ocean ridge magma chambers are elongated, narrow features (e.g., [39]). Misalignment of the MCS sources and receivers over the center of the AMC, or drift of the hydrophone streamer (feathering), may affect both imaging [40] and waveform modeling of the AMC. In our experiment, streamer feathering was small ( $\sim 7^\circ$  and  $\sim 4^\circ$  at the location of CMP 2200 in N-Cleft and CMP 8200 in S-Cleft, respectively). This small feathering results in a maximum deviation of the CMP location for the far-offset traces of  $\sim 210\text{--}370$  m from the assumed straight line, which is smaller than, or of similar magnitude as the half-width of the AMC in this area (300–850 m [3]). Thus feathering does not

seem to introduce significant bias in our results. The importance of other factors such as lateral variability within the AMC at scales smaller than the seismic footprint (Fresnel zone), or differences in upper crustal properties such as density or attenuation between both sites, cannot be assessed in our simplified 1D approach.

#### 4. Partial-offset $S$ -wave stacking

Singh et al. [16] have shown that at the southern EPR, converted  $S$ -waves reflecting off the AMC can be imaged along the axis using conventional seismic reflection imaging techniques. In our data, coherent events that could be attributed to these converted  $S$ -wave reflections are not easily recognized in the super-CMP gathers because the data suffer from the presence of noise originated from side-echos due to the rough seafloor topography (Fig. 2a, b). However this unwanted energy can be partially removed by dip filtering the super-CMP gathers in the frequency-wavenumber domain ( $f-k$ ). One important advantage of using super-CMP gathers is that the smaller source-receiver offset step (12.5 m in super-CMP gathers versus 75 m in a CMP gather) allows for higher frequency signals to be dip filtered without spatial aliasing. After applying an  $f-k$  filter that suppresses energy with apparent velocities lower than 4.1 km/s, super-CMP 2200 shows a coherent event between 2 and 5 km offset at 4.5–4.8 s twtt ( $P_{AMC}S$ , Fig. 4a) that was not clearly observed in the unfiltered gather (Fig. 2a). We explored different possible origins for this event, and found that its travel time (Fig. 4b) is consistent with a conversion from an incident  $P$ - to an  $S$ -wave reflected at the top of the AMC (and then converted back to  $P$ -wave at the seafloor). The reflection coefficient for the  $P_{AMC}S$  event in the case of a mush-rich magma chamber ( $V_S > 0$  km/s) shows that for offsets larger than 2 km, the  $P_{AMC}S$  event should have an amplitude comparable to the reflected  $P$ -wave ( $P_{AMC}P$ ) (Fig. 4c). Here we prefer to use the name of  $P_{AMC}S$  (instead of  $P_{melt}S$ , as in Singh et al. [16]) to emphasize that this event could be observed even in the case when the AMC is not totally molten. Other possible origins for the  $P_{AMC}S$  event, such as a pegleg multiple from layer 2A or an  $S$ -wave conversion at the base of layer 2A, do not predict the observed travel-time variation with offset.

The  $P_{AMC}S$  event can be processed and imaged as another reflector in conventional reflection imaging. We have produced a seismic reflection stack (hereinafter referred to as partial-offset  $S$ -wave stack) to image the  $P_{AMC}S$  event along the axis of the Cleft segment to understand its relationship to the  $P_{AMC}P$  event (i.e., the

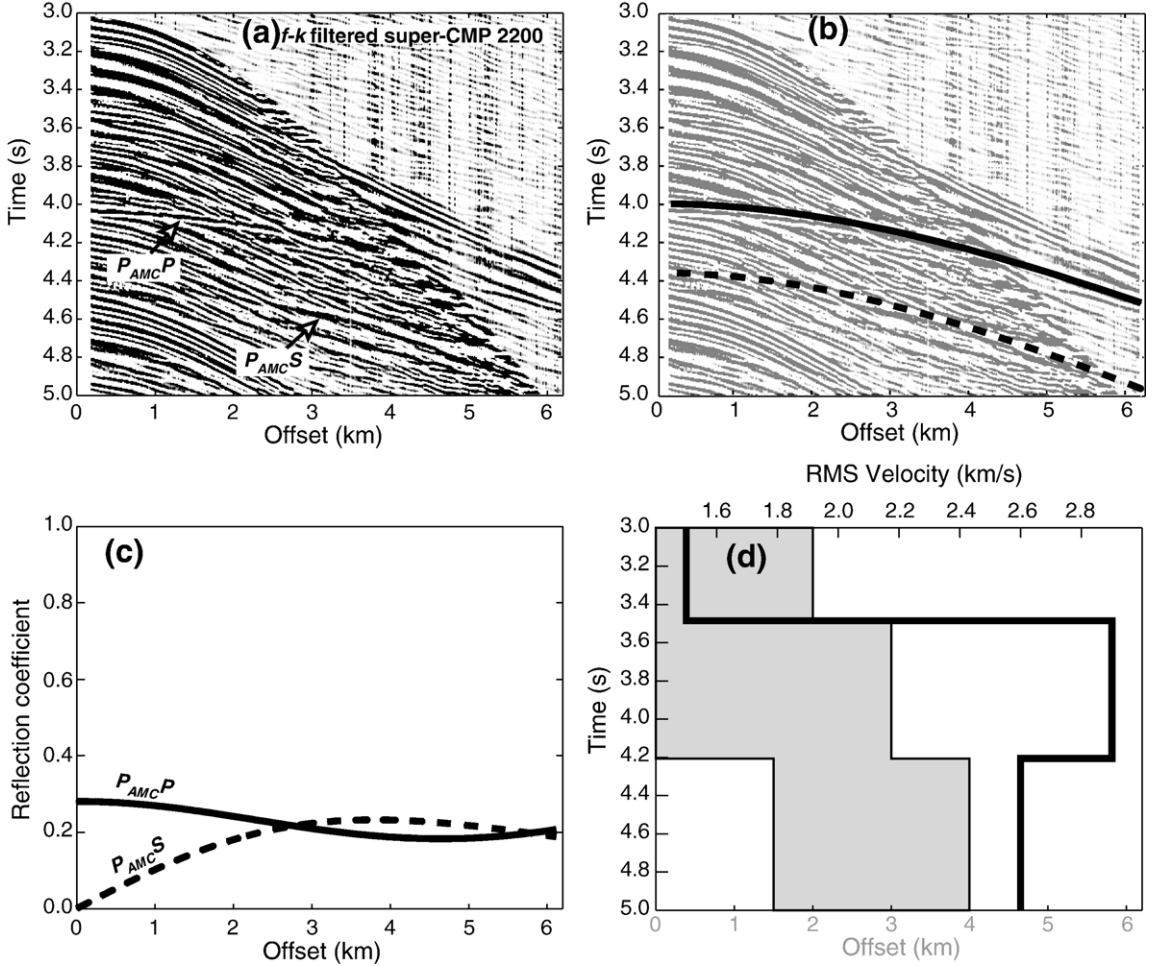


Fig. 4. (a)  $f-k$  filtered super-CMP 2200 (events with apparent velocity  $<4.1$  km/s have been filtered) showing the  $P$ -wave ( $P_{AMC}P$ ) and converted  $S$ -wave ( $P_{AMC}S$ ) AMC reflections. (b) Same as (a) with predicted travel-time curves for both events. (c) Theoretical  $P$ -wave (solid) and  $S$ -wave (dashed) reflection coefficients versus offset for a  $P$ -wave incident in a half space (upper layer:  $V_P=6.0$  km/s,  $V_S=3.2$  km/s,  $\rho=2700$  kg/m $^3$ ; bottom layer:  $V_P=3.5$  km/s,  $V_S=2.0$  km/s,  $\rho=2600$  kg/m $^3$ ). (d) Offset-dependent surgical mute (gray area, bottom horizontal axis) applied after NMO, and the RMS velocity function (solid line, top horizontal axis) versus time used for NMO.

AMC reflector of Canales et al. [3]) and determine the along-axis variability of the AMC properties. The steps followed to create the  $S$ -wave stack are: (1) 480-fold super-CMP gathers (as described in Section 2) were created at each CMP location along the seismic profile Line 80 collected along the axis of Cleft [3]; (2) amplitude scaling by automatic gain control (AGC); (3)  $f-k$  filtering of the super-CMP gathers as described above; (4) amplitude de-scaling (AGC removed); (5) normal move-out (NMO) correction using a simple, three-layer RMS velocity function (Fig. 4d): 1.5 km/s for the seafloor reflection, 2.9 km/s for the  $P$ -wave, and 2.6 km/s for the  $S$ -wave (note that for simplicity we have not included appropriate velocities to image the base of layer 2A, which has already been described in detail by

Canales et al. [3]); (6) surgical mute to select the offsets were the  $P_{AMC}P$  and  $P_{AMC}S$  events are most prominent (Fig. 4d); and (7) stack of the NMO-corrected, muted super-CMP gathers.

The partial-offset  $S$ -wave stack is shown in Fig. 5. The  $P$ -wave reflection from the AMC is observed at  $\sim 4$  s two-way travel time along most of the axis of Cleft, consistent with the previous migrated images of Canales et al. [3]. The  $S$ -wave reflection can be observed at  $\sim 4.5$  s, but only along the northern half section of the Cleft segment: between  $44^{\circ}52'N$  and  $44^{\circ}53'N$ , near  $44^{\circ}54.6'N$ , and between  $44^{\circ}57.5'N$  and  $44^{\circ}59.5'N$ . While other reflections of similar characteristics are present at similar depths at other parts of the segment, they are more ambiguous and lack the

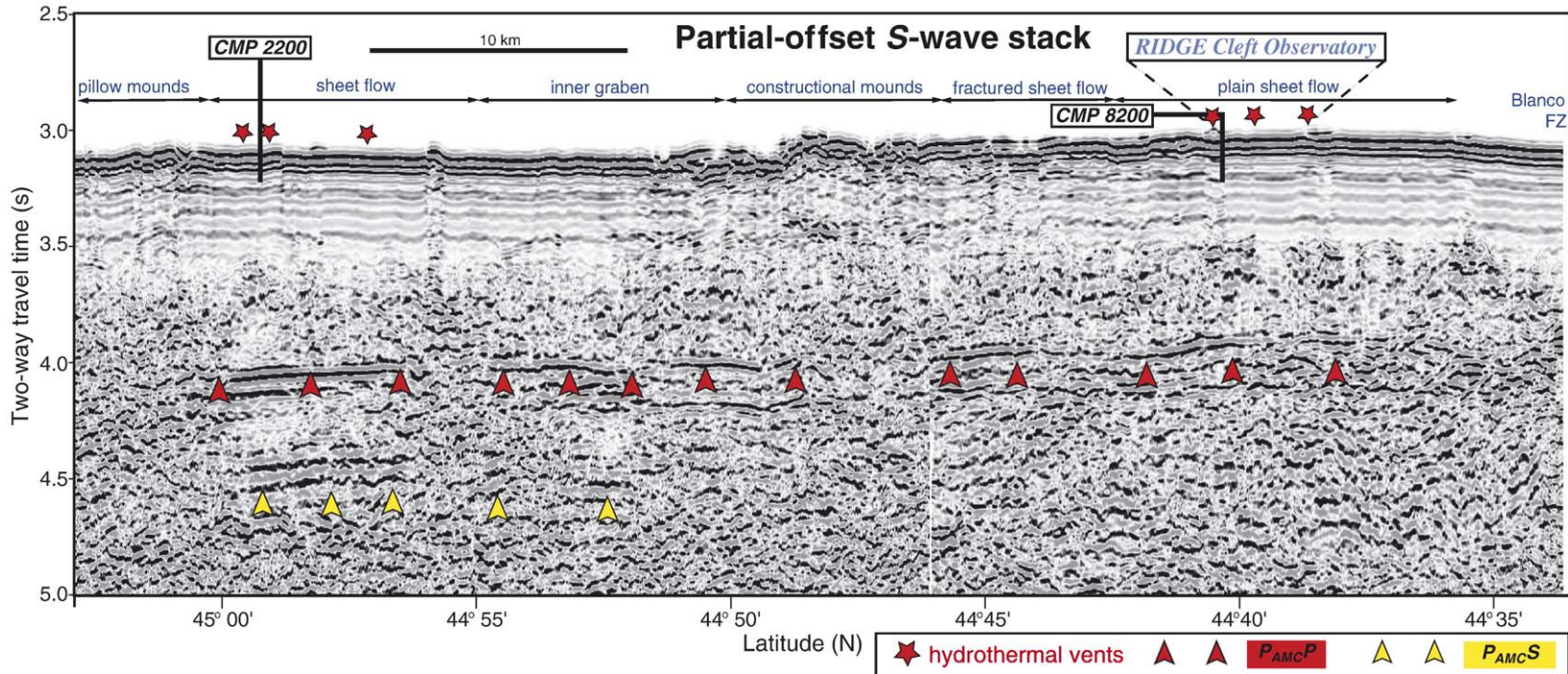


Fig. 5. Partial-offset S-wave stack along the axis of the Cleft segment, showing the  $P_{AMC}P$  and  $P_{AMC}S$  events. Note that the  $P_{AMC}S$  event is only present beneath the AMC at the northern end of the segment, but it is absent anywhere else (except possibly near 44°52'N). Lava morphologies are from Embley and Chadwick [19].

lateral continuity of the  $P_{AMC}S$  events mentioned above, so we will not attempt to interpret them. A confirmation that the  $P_{AMC}S$  event is related to the AMC is that we only image it where the AMC  $P$ -wave reflection is strongest (Fig. 5). If it was an imaging artifact or related to other crustal structures, we would not find such clear correlation.

## 5. Discussion

### 5.1. Nature of the axial mid-crustal reflector at intermediate-spreading ridges

Wilcock and Delaney [13] propose that the mechanism of heat extraction by hydrothermal circulation at mid-ocean ridges is fundamentally different between fast- and slow-spreading ridges. At fast-spreading ridges like the EPR, hydrothermal circulation at the ridge axis is confined above a thin melt lens seismically characterized by a significant decrease in seismic velocity (e.g., [16]). At slow-spreading ridges, Wilcock and Delaney [13] suggest that hydrothermal circulation extracts heat by means of a downward propagating cracking front into hot but un-molten rock, due to tectonic extension that keeps fluid paths open and ephemeral crustal magma bodies. The seismic signature of such a front would be a small increase in seismic velocity. Wilcock and Delaney [13] argue that at intermediate-spreading ridges like the JdFR the mechanism of heat extraction will vary between both end members, depending on the tectonomagmatic state of the ridge.

van Ark et al. [41] have recently shown that the mid-crustal reflector beneath the Endeavour segment at the northern end of the JdFR has many of the characteristics of a partially molten AMC, and rejected the hypothesis of a cracking front. However, these authors did not provide the detailed seismic structure of the AMC. Here we have shown that at the intermediate-spreading Cleft segment, the seismic structure of the AMC is very similar to that found along the EPR. It is ~100 m thick and has low  $P$ -wave velocity. The reduction in seismic velocity within the AMC is indicative of its molten state. Furthermore, based on resolution tests (Fig. 3) we argue that the melt lens is thin and it is underlain by a mostly crystallized floor, where most of the crystallization takes place due to cooling within a convecting magma chamber [42]. Thus our results, together with those of van Ark et al. [41], indicate that mid-crustal axial reflectors along intermediate-spreading ridges are of the same nature as those found along fast-spreading ridges, i.e., thin melt lenses, and not propagating cracking fronts.

### 5.2. Variations in AMC properties: implications for magmatic processes

Our results on the  $P$ -wave velocity structure of the AMC provide constraints on the crystallinity of the melt lens. To estimate the melt content in the AMC we used the relationship derived from effective medium theory between the composition and microstructure of a melt body, and its seismic properties [43]. Fig. 6 shows the melt content of the AMC at both sites along the Cleft segment that is consistent with our  $P$ -wave velocity models, for different microstructures ranging from isolated crystals suspended in a melt matrix to isolated melt inclusions embedded in a solid matrix. At the northern site, the low  $V_P$  (3.7 km/s) indicates that the AMC has a larger percentage of melt (60–75%). In contrast, at the southern site the larger  $V_P$  (5.0 km/s) is consistent with a magma body with low melt content (<30%).

These two estimates of the crystallinity of the AMC, together with the S-wave stack, provide a more complete picture about the present properties of the AMC and their along-axis variations. Along the southern part of the Cleft segment, between ~44°38'–46°N, the AMC ( $P_{AMC}P$  event) is well imaged (Figs. 5 and 7c), but the  $P_{AMC}S$  event is absent. The waveform inversion results at CMP 8200 near 44°40'N indicate that at this location the AMC has a small percentage of melt content. Therefore, we can infer that along the southern half of the Cleft segment the axial magma chamber is mostly crystallized, with a maximum of 30% of melt in it. In contrast, in the vicinity of CMP 2200 near 44°59'N, where the velocity model indicates a high melt content in the AMC, the  $P_{AMC}S$  event is strongest and laterally

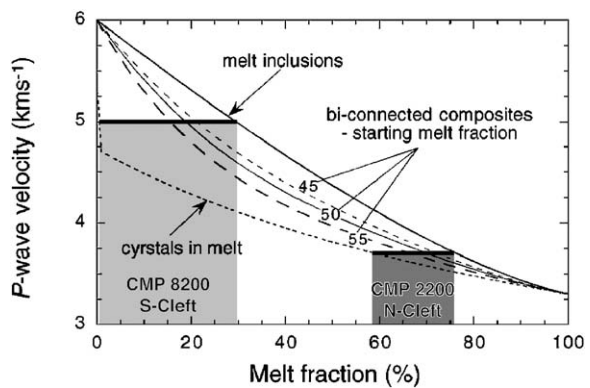


Fig. 6. Variation in  $P$ -wave velocity with melt fraction for spherical inclusions and different microstructures (figure modified from Taylor and Singh [43]).  $P$ -wave velocities are consistent with 60–75% melt (dark gray) and less than 30% melt (light gray) in the AMC at N-Cleft and S-Cleft, respectively.

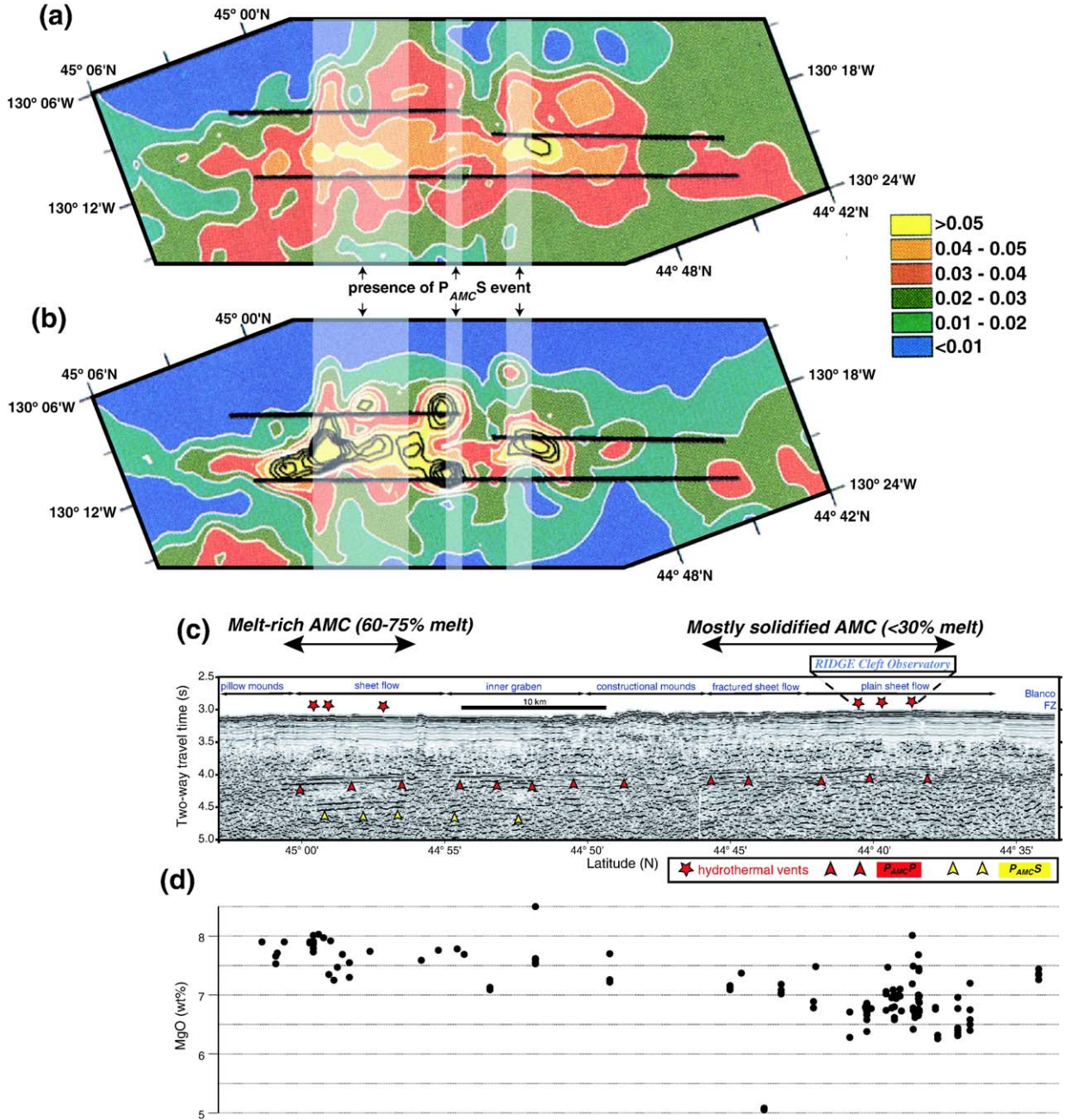


Fig. 7. Maps of maximum (a) temperature and (b) light attenuation anomalies from hydrothermal plumes (modified from Baker [48]). Color scale corresponds to temperature anomaly in °C in (a) and to light attenuation anomaly in m<sup>-1</sup> in (b). Shaded vertical bars indicate the areas along the ridge where the  $P_{AMC}S$  event is observed. Horizontal solid lines delineate the limits of the axial summit graben. (c) Partial-offset S-wave stack along the axis of the Cleft segment as in Fig. 5. Note the excellent spatial correlation between the  $P_{AMC}S$  event and the location of hydrothermal plumes inferred from the temperature and light attenuation maps. (d) MgO content of axial lavas along the Cleft segment. Data from the RIDGE Petrological Database [29,53–57]. Note the good spatial correlation between the presence of the  $P_{AMC}S$  event and the more primitive (higher MgO) lavas.

continuous, suggesting that along this section of the northern part of the segment the AMC is more melt-rich, with 60–75% melt content in it. Along the center of the segment between these two areas of contrasting

crystallinity, the AMC probably has some intermediate properties, as suggested by the small  $P_{AMC}S$  event observed near 44°52'N (Figs. 5 and 7c). Based on the melt content inferred from the seismic properties, an

eruption along the northern part of the Cleft segment is more likely to happen than at the southern end near the RIDGE Cleft Observatory.

The variations in AMC properties that we have inferred from the seismic data agree with the existing petrological data along the axis of Cleft (e.g., [29]). Along the southern half of the segment where the  $P_{AMCS}$  event is absent and the AMC  $P$ -wave velocity is higher, lavas are moderate to highly evolved, with low MgO wt.% (average of  $6.8 \pm 0.3$  wt.%) indicative of a cooler crustal reservoir (Fig. 7d) [29]. In contrast, along the northern part of the segment where the  $P_{AMCS}$  event is best imaged and the AMC is characterized by a more pronounced decrease in  $P$ -wave velocity, lavas are more mafic and primitive, with higher MgO wt.% (average of  $7.6 \pm 0.3$  wt.%) [29] indicative of a hotter crustal reservoir (Fig. 7d). Smith et al. [29] attributed the changes in lava chemistry along the axis of Cleft to eruptions from discrete magma lenses in different stages of evolution, without significant along-axis transport of magma. Our results agree with this interpretation. The seismic properties of the AMC that we have inferred suggest that the top of the AMC is segmented in 5- to 10-km-long melt lenses with distinct properties, becoming more melt rich towards the north.

A striking result is that the northward increase in melt content within the AMC and the increase in the mafic nature of the lavas are both accompanied by an increase in AMC depth [3] (Figs. 3 and 5). Along mid-ocean ridges, the level of magma accumulation (i.e., AMC depth) is not a neutral buoyancy level [44]. Instead, it is controlled by the thermal structure of the ridge axis, possibly being the brittle–ductile boundary (e.g., [45]) or a freezing horizon (e.g., [46]). Since the top of the AMC should correspond to the solidus temperature, one would expect that the hotter AMC along the northern end of Cleft that has the lowest  $P$ -wave velocity, and from which the most primitive lavas erupted, would lie at shallower levels than the cooler, higher  $P$ -wave velocity AMC at the southern end of the segment. This apparent contradiction thus suggests that the crustal thermal regime that controls the depth of the AMC (e.g., [46,47]) must take time to re-equilibrate after new heat input by the injection of magma from the mantle to the crust. A 100-m-thick melt lens takes 150–200 yr to crystallize (assuming no new magma input) [42]. If the process of replenishment of the AMC is not continuous and occurs episodically at intervals longer than  $\sim 200$  yr, then the southern Cleft could be in a state where most of the melt from the shallow AMC has crystallized and/or been extracted and it has

not yet received a new input of fresh magma. Thus the shallower AMC indicates that the thermal structure at the southern Cleft has not reached a thermal equilibrium to compensate this deficit of heat after the latest eruptions in this area. In contrast, at the northern Cleft, the regional crustal thermal regime is somewhat cooler than at the southern Cleft (thus the deeper AMC), but the axial melt lens has not yet been fully crystallized since the last replenishment and/or it was not completely drained of magma during the last eruption. However one must note that the difference in AMC depth between the southern and northern Cleft is only 300 m. At the intermediate spreading rate of the Cleft segment, this small difference can be produced by very subtle differences in crustal thermal structure [11].

### 5.3. Correlations between AMC seismic properties and hydrothermal activity

Plume temperature anomalies in the water column are useful indicators of the relative strength of hydrothermal heat sources [48]. Along the southern EPR, Singh et al. [15] found that the magmatic segmentation of the AMC (i.e., melt-rich sections of the AMC) correlates with the location of hydrothermal plumes. We find a similar correlation along the Cleft segment. Fig. 7a and b show maps of maximum temperature and light attenuation anomalies along the axis of the Cleft segment, compiled from plume data collected between 1986 and 1991 [48]. Although the details of these temperature and light attenuation anomalies differ from year to year, these maps emphasize the features that were consistent during the several-year observation period, in particular the location of chronic plumes [48]. The plumes have a strong spatial correlation with the presence of the  $P_{AMCS}$  event, specially the light attenuation anomalies (Fig. 7). Even the discrete  $P_{AMCS}$  event near  $44^{\circ}52'N$  directly correlates with an isolated plume anomaly at this location along the segment.

Both of the known hydrothermal vent fields along Cleft are underlain by an axial magma chamber reflector (Figs. 5 and 7c [3]), indicating that along this segment high-temperature venting is focused directly above a steady-state magmatic heat source. However, only at the northern hydrothermal vent field do we observe a clear  $P_{AMCS}$  event. Unfortunately plume data coverage from the southern Cleft is not as complete as in the northern area [48]. There are no similar plan view maps of temperature and/or light attenuation anomalies for the southern end the Cleft segment in the published literature, preventing us from

testing whether or not the absence of the  $P_{AMC}S$  event at the southern vents site also correlates with well-defined plume anomalies. However, the available data indicates that hydrothermal plume anomalies along the axis of southern Cleft are not as pronounced as that of northern Cleft [49], supporting the idea that hydrothermal plume anomalies are stable over periods of at least several years, and thus the style of focused, high-temperature venting at intermediate-spreading ridges, is closely linked to the physical state of the underlying magma chamber.

Baker and Hammond [49] suggested that hydrothermal activity along the JdFR followed the tectono-magmatic episodicity postulated by Kappel and Ryan [50], with hydrothermal activity reflecting the distribution of current magmatic heat sources. However, new observations show that all of the JdFR segments are in a magmatic state (i.e., underlain by an AMC reflector) [51], arguing against the tectono-magmatic model of Kappel and Ryan [50]. The observations and correlations presented in this paper indicate that, while high-temperature hydrothermal activity is clearly linked to the presence of an AMC, only those sections of the ridge with high melt content are able to support vents that result in consistent plume anomalies detectable over several-year time scales.

## 6. Conclusions

1. Waveform modeling of the mid-crustal reflector observed along the axis of the intermediate-spreading Cleft segment at the southern Juan de Fuca Ridge indicates that this reflector arises from a significant decrease in  $P$ -wave velocity at the top of a partially molten magma chamber, therefore excluding the possibility that it could represent another type of structure such as a downward-propagating cracking front.
2. At the southern end of the segment (RIDGE Cleft Observatory) beneath high-temperature hydrothermal vents, the AMC is shallower (1.9 km) and the  $P$ -wave velocity within the AMC (5.0 km/s) indicates less than 30% melt content. In contrast, the AMC beneath the northern hydrothermal vents is deeper (2.23 km) but it has a lower  $V_p$  (3.7 km/s), and therefore it is more melt rich (60–75%).
3. Converted  $S$ -waves at the top of the AMC ( $P_{AMC}S$ ) mapped along the segment, together with the melt content estimates, indicate that the crystallinity of the AMC varies along axis, from a low melt content or mostly solidified AMC along the southern half of Cleft, to a melt-rich magma chamber along the

northern half of the segment. These variations in seismic properties are accompanied by a northward increase in MgO in erupted lavas, corroborating previous hypothesis that eruptions along the Cleft segment occur from magma chambers in different stages of evolution.

4. The observation that the AMC is deeper where lavas are more primitive and the melt content is higher indicates that eruption from and replenishment of the AMC must occur at shorter time intervals than the time needed for the regional thermal regime (that controls the depth of the AMC) to re-equilibrate after most of the magma from the top of the AMC has been erupted or crystallized.
5. We also find good correlations between the presence of the  $P_{AMC}S$  event (hotter AMC) and the location of hydrothermal plumes. This suggests that the style of focused, high-temperature venting at intermediate-spreading ridges is closely linked to the physical state of the underlying magma chamber.

## Acknowledgments

This study was supported by the National Science Foundation grants OCE-0002551 to Woods Hole Oceanographic Institution, OCE-0002488 to Lamont-Doherty Earth Observatory, and OCE-0002600 to Scripps Institution of Oceanography. We are grateful to Captain Mark Landow, Science Officer Joe Stennet, and the crew and scientific and technical party of the R/V *Maurice Ewing* Cruise 02-07 for their support and help during the data acquisition. We thank T. Minshull for his constructive review, which helped to improve the original manuscript. Some of the figures were prepared with GMT software [52]. Seismic data was processed with Focus software by Paradigm.

## References

- [1] T.M. Blacic, G. Ito, J.P. Canales, R.S. Detrick, J.M. Sinton, Constructing the crust along the Galapagos Spreading Center 91.3°–95.5°W: correlation of seismic layer 2A with axial magma lens and topographic characteristics, *J. Geophys. Res.* 109 (2004) B10310, doi:10.1029/2004JB003066.
- [2] J.M. Baran, J.R. Cochran, S.M. Carbotte, M.R. Nedimović, Variations in upper crustal structure due to variable mantle temperature along the Southeast Indian Ridge, *Geochem. Geophys. Geosyst.* 6 (2005) Q11002, doi:10.1029/2005GC000943.
- [3] J.P. Canales, R.S. Detrick, S.M. Carbotte, G.M. Kent, J.B. Diebold, A.J. Harding, J. Babcock, M.R. Nedimović, E. van Ark, Upper crustal structure and axial topography at intermediate-spreading ridges: seismic constraints from the Southern Juan de Fuca Ridge, *J. Geophys. Res.* (2005) B12104, doi:10.1029/2005JB003630.

- [4] J.L. Morton, N.H. Sleep, W.R. Normark, D.H. Tompkins, Structure of the southern Juan de Fuca Ridge from seismic reflection records, *J. Geophys. Res.* 92 (1987) 11,315–11,326.
- [5] K.M.M. Rohr, B. Milkereit, C.J. Yorath, Asymmetric deep crustal structure across the Juan de Fuca Ridge, *Geology* 16 (1988) 533–537.
- [6] J.L. Morton, N.H. Sleep, Seismic reflections from a Lau Basin magma chamber, in: D.W. Scholl, T.L. Vallier (Eds.), *Geology and Offshore Resources of Pacific Island Arcs—Tonga Region*, Earth Sciences Series, vol. 2, Circum-Pacific Council for Energy and Mineral Resources, Houston, TX, 1985, pp. 441–453.
- [7] J.S. Collier, M.C. Sinha, Seismic images of a magma chamber beneath the Lau Basin back-arc spreading center, *Nature* 346 (1990) 646–648.
- [8] R.S. Detrick, P. Buhl, E.E. Vera, J.C. Mutter, J.A. Orcutt, J.A. Madsen, T.M. Brocher, Multi-channel seismic imaging of a crustal magma chamber along the East Pacific Rise, *Nature* 326 (1987) 35–41.
- [9] J.S. Collier, M.C. Sinha, Seismic mapping of a magma chamber beneath the Valu Fa Ridge, Lau Basin, *J. Geophys. Res.* 97 (1992) 14,031–14,053.
- [10] W.S.D. Wilcock, S.D. Archer, G.M. Purdy, Microearthquakes on the Endeavour segment of the Juan de Fuca Ridge, *J. Geophys. Res.* 107 (2002) 2336, doi:10.1029/2001JB000505.
- [11] J. Phipps Morgan, Y.J. Chen, Dependence of ridge-axis morphology on magma supply and spreading rate, *Nature* 364 (1993) 706–708.
- [12] J.M. Sinton, R.S. Detrick, Mid-ocean ridge magma chambers, *J. Geophys. Res.* 97 (1992) 197–216.
- [13] W.S.D. Wilcock, J.R. Delaney, Mid-ocean ridge sulfide deposits: evidence for heat extraction from magma chambers or cracking fronts? *Earth Planet. Sci. Lett.* 145 (1996) 49–64.
- [14] S.A. Hussenhoeder, J.A. Collins, G.M. Kent, R.S. Detrick, the TERA Group, Seismic analysis of the axial magma chamber reflector along the southern East Pacific Rise from conventional reflection profiling, *J. Geophys. Res.* 101 (1996) 22,087–22,105.
- [15] S.C. Singh, J.S. Collier, A.J. Harding, G.M. Kent, J.A. Orcutt, Seismic evidence for a hydrothermal layer above the solid roof of the axial magma chamber at the southern East Pacific Rise, *Geology* 27 (1999) 219–222.
- [16] S.C. Singh, G.M. Kent, J.S. Collier, A.J. Harding, J.A. Orcutt, Melt to mush variations in crustal magma properties along the ridge crest at the southern East Pacific Rise, *Nature* 394 (1998) 874–878.
- [17] J.S. Collier, S.C. Singh, Detailed structure of the top of the melt body beneath the East Pacific Rise at 9°40'N from waveform inversion of seismic reflection data, *J. Geophys. Res.* 102 (1997) 20,287–20,304.
- [18] D.S. Wilson, Confidence intervals for motion and deformation of the Juan de Fuca plate, *J. Geophys. Res.* 98 (1993) 16,053–16,071.
- [19] R.W. Embley, W.W. Chadwick, Volcanic and hydrothermal processes associated with a recent phase of seafloor spreading at the northern Cleft segment: Juan de Fuca Ridge, *J. Geophys. Res.* 99 (1994) 4741–4760.
- [20] W.R. Normark, J.L. Morton, R. Koski, D.A. Clague, Active hydrothermal vents and sulfide deposits on the southern Juan de Fuca Ridge, *Geology* 11 (1983) 158–163.
- [21] W.R. Normark, J.L. Morton, J.L. Bischoff, R.T. Holcomb, E.S. Kappel, R. Koski, S.L. Ross, W.C. Shanks III, J.F. Slack, K.L. Von Damm, R.A. Zierenburg, Submarine fissure eruptions and hydrothermal vents on the southern Juan de Fuca Ridge: preliminary observations from the submersible *Alvin*, *Geology* 14 (1986) 823–827.
- [22] W.W. Chadwick, D.S. Scheirer, R.W. Embley, H.P. Johnson, High-resolution bathymetric surveys using scanning sonars: lava flow morphology, hydrothermal vents, and geologic structure at recent eruption sites on the Juan de Fuca Ridge, *J. Geophys. Res.* 106 (2001) 16,075–16,099.
- [23] D.J. Fornari, R.M. Haymon, M.R. Perfit, T.K.P. Gregg, M.H. Edwards, Axial summit trough of the East Pacific Rise 9°–10°N: geological characteristics and evolution of the axial zone on fast spreading mid-ocean ridges, *J. Geophys. Res.* 103 (1998) 9827–9855.
- [24] K.C. Macdonald, P.J. Fox, The axial summit graben and cross-sectional shape of the East Pacific Rise as indicators of axial magma chambers and recent volcanic eruptions, *Earth Planet. Sci. Lett.* 88 (1988) 119–131.
- [25] C.D. Chadwell, J.A. Hildebrand, F.N. Spiess, J.L. Morton, W.R. Normark, C.A. Reiss, No spreading across the southern Juan de Fuca ridge axial Cleft during 1994–1996, *Geophys. Res. Lett.* 26 (1999) 2525–2528.
- [26] W.W. Chadwick, E.T. Baker, D.A. Butterfield, J.P. Canales, S.M. Carbotte, D.W. Caress, C.D. Chadwell, R.S. Detrick, J.B. Diebold, A.J. Harding, J.A. Hildebrand, H.W. Jannasch, K. Johnson, G.M. Kent, R. Koski, J.L. Morton, W.R. Normark, M.R. Perfit, C.A. Reiss, G.S. Sasagawa, M. Smith, F.N. Spiess, D.S. Stakes, M.A. Tivey, S. Tucker, C.G. Wheat, M.A. Zumberge, The RIDGE Observatory at the Cleft segment: investigation of linkages between geodetic, geophysical, geochemical, and water column processes, *RIDGE Events* 11 (2001) 18–24.
- [27] W.W. Chadwick, R.W. Embley, C.G. Fox, Evidence for volcanic eruptions on the southern Juan de Fuca Ridge between 1981 and 1987, *Nature* 350 (1991) 416–418.
- [28] R.W. Embley, J. Chadwick, W. William, M.R. Perfit, E.T. Baker, Geology of the northern Cleft segment, Juan de Fuca Ridge: recent lava flows, sea-floor spreading, and the formation of megaplumes, *Geology* 19 (1991) 771–775.
- [29] M.C. Smith, M.R. Perfit, I.R. Jonasson, Petrology and geochemistry of basalts from the southern Juan de Fuca Ridge: controls on the spatial and temporal evolution of mid-ocean ridge basalt, *J. Geophys. Res.* 99 (1994) 4787–4812.
- [30] M.R. Perfit, D.S. Stakes, M.A. Tivey, S.E. Kulp, W.I. Ridley, T. M. Ramirez, Magma genesis and crustal formation along the southern Juan de Fuca Ridge (JdFR): results of fine-scale sampling and mapping, *Geophys. Res. Abstr.* 5 (2003) 07287.
- [31] A.J. Harding, Slowness-time mapping of near offset seismic reflection data, *Geophys. J. R. Astron. Soc.* 80 (1985) 463–492.
- [32] J. Korenaga, W.S. Holbrook, S.C. Singh, T.A. Minshull, Natural gas hydrates on the southeast U.S. margin: constraints from full waveform and travel time inversions of wide-angle seismic data, *J. Geophys. Res.* 102 (1997) 15,345–15,365.
- [33] T.A. Minshull, S.C. Singh, G.K. Westbrook, Seismic velocity structure at a gas hydrate reflector, offshore western Columbia, from full waveform inversion, *J. Geophys. Res.* 99 (1994) 4715–4734.
- [34] F. Kormendi, M. Dietrich, Nonlinear waveform inversion of plane-wave seismograms in stratified elastic media, *Geophysics* 56 (1991) 664–674.
- [35] R.L. Carlson, G.S. Raskin, Density of the oceanic crust, *Nature* 311 (1984) 555–558.
- [36] L.A. Gilbert, H.P. Johnson, Direct measurement of oceanic crustal density at the northern Juan de Fuca Ridge, *Geophys. Res. Lett.* 26 (1999) 3633–3636.

- [37] G.L. Christeson, P.R. Shaw, J.D. Garmany, Shear and compressional wave structure of the East Pacific Rise, 9°–10°N, *J. Geophys. Res.* 102 (1997) 7821–7835.
- [38] G.L. Christeson, W.S.D. Wilcock, G.M. Purdy, The shallow attenuation structure of the fast-spreading East Pacific Rise near 9°30'N, *Geophys. Res. Lett.* 21 (1994) 321–324.
- [39] G.M. Kent, A.J. Harding, J.A. Orcutt, Evidence for a smaller magma chamber beneath the East Pacific Rise at 9°30'N, *Nature* 344 (1990) 650–653.
- [40] M.R. Nedimović, S. Mazzotti, R.D. Hyndman, Three-dimensional structure from feathered two-dimensional marine seismic reflection data: the eastern Nankai Trough, *J. Geophys. Res.* 108 (2003) 2456, doi:10.1029/2002JB001959.
- [41] E. van Ark, R.S. Detrick, J.P. Canales, S.M. Carbotte, J.B. Diebold, A.J. Harding, G.M. Kent, M.R. Nedimović, W.S.D. Wilcock, Seismic structure of the Endeavour segment, Juan de Fuca Ridge: correlations of crustal magma chamber properties with seismicity, faulting, and hydrothermal activity, *Eos Trans. AGU* 84 (2003) (Fall Meet. Suppl., B12A-0752).
- [42] M.G. Worster, H.E. Huppert, R.S.J. Sparks, Convection and crystallization in magma cooled from above, *Earth Planet. Sci. Lett.* 101 (1990) 78–89.
- [43] M.A.J. Taylor, S.C. Singh, Compositions and microstructure of magma bodies from effective medium theory, *Geophys. J. Int.* 149 (2002) 15–21.
- [44] E. Hooft, R.S. Detrick, The role of density in the accumulation of basaltic melts at mid-ocean ridges, *Geophys. Res. Lett.* 20 (1993) 423–426.
- [45] A.M. Rubin, A comparison of rift-zone tectonics in Iceland and Hawaii, *Bull. Volcanol.* 52 (1990) 302–319.
- [46] J. Phipps Morgan, Y.J. Chen, The genesis of oceanic crust: magma injection, hydrothermal circulation, and crustal flow, *J. Geophys. Res.* 98 (1993) 6283–6297.
- [47] D. Sparks, E.M. Parmentier, Melt extraction from the mantle beneath spreading centers, *Earth Planet. Sci. Lett.* 105 (1991) 368–377.
- [48] E.T. Baker, A 6-year time series of hydrothermal plumes over the Cleft segment of the Juan de Fuca Ridge, *J. Geophys. Res.* 99 (1994) 4889–4904.
- [49] E.T. Baker, S. Hammond, Hydrothermal venting and the apparent magmatic budget of the Juan de Fuca Ridge, *J. Geophys. Res.* 97 (1992) 3443–3456.
- [50] E.S. Kappel, W.B.F. Ryan, Volcanic episodicity and a non-steady state rift valley along the Northeast Pacific spreading centers: evidence from Sea MARC I, *J. Geophys. Res.* 91 (1986) 13,925–13,940.
- [51] S.M. Carbotte, R.S. Detrick, A.J. Harding, J.P. Canales, J. Babcock, G.M. Kent, E. van Ark, M.R. Nedimović, J.B. Diebold, Rift topography linked to magmatism at the intermediate spreading Juan de Fuca Ridge, *Geology* 34 (2006) 209–212.
- [52] P. Wessel, W.H.F. Smith, New version of the generic mapping tools released, *Eos Trans. AGU* 76 (1995) 329.
- [53] J.S. Eaby, D.A. Clague, J.R. Delaney, Sr isotopic variations along the Juan de Fuca Ridge, *J. Geophys. Res.* 89 (1984) 7883–7890.
- [54] D.M. Christie, I. Carmichael, C.H. Langmuir, Oxidation states of mid-ocean ridge basalt glasses, *Earth Planet. Sci. Lett.* 79 (1986) 397–411.
- [55] J.E. Dixon, D.A. Clague, J.-P. Eissen, Gabbroic xenoliths and host ferrobasalts from the southern Juan de Fuca Ridge, *J. Geophys. Res.* 91 (1986) 3795–3820.
- [56] G. Fine, E.M. Stolper, Dissolved carbon dioxide in basalt glasses: concentrations and speciation, *Earth Planet. Sci. Lett.* 76 (1985) 263–278.
- [57] J.G. Ryan, C.H. Langmuir, The systematics of lithium abundances in young volcanic rocks, *Geochim. Cosmochim. Acta* 51 (1987) 1727–1741.